

Detecting overlapping gravity waves using the S-Transform

C. J. Wright¹ and J. C. Gille^{1,2}

Received 18 December 2012; revised 13 March 2013; accepted 16 March 2013.

[1] We discuss an adaptation to the widely-used Stockwell Transform based method for the detection of gravity waves to allow the detection of multiple overlapping waves. This adjusted method is applied to data from the High Resolution Dynamics Limb Sounder for the period of May 2006 and is found to change the measured distribution of gravity wave momentum flux on a global scale. An overall 68% increase in measured momentum flux is observed for the 20–30 km altitude range, with significant regional variability. The largest absolute increase is over India, the Southern Ocean, and the Antarctic Peninsula, regions previously known to exhibit high levels of momentum flux. A strong relative increase is observed north of the equator, particularly in the tropics; analysis of the wavelength distribution of detected gravity waves shows that the majority of this increase is due to the detection of small vertical- and horizontal-scale waves which were presumably previously masked by higher-amplitude events in the same profile. **Citation:** Wright, C. J., and J. C. Gille (2013), Detecting overlapping gravity waves using the S-Transform, *Geophys. Res. Lett.*, *40*, doi:10.1002/grl.50378.

1. Introduction

[2] Gravity waves (GWs) are a key component in our understanding of the global atmospheric circulation, helping to determine the broad-scale structure of the middle atmosphere and driving atmospheric dynamics on all scales [Fritts, 1984]. Recent advances in satellite instrumentation [e.g., Fritts and Alexander, 2003; Alexander *et al.*, 2010] have allowed their direct measurement at high resolution on a global scale, facilitating the mapping and characterization of their distribution. This detailed understanding is vitally important to provide necessary observational constraints for the GW parameterizations which form a key component of climate and weather models. [e.g., Song *et al.*, 2007; Richter *et al.*, 2010]

[3] In recent years, the Stockwell Transform (ST, Stockwell *et al.*, [1996]) has been widely used to infer the vertical flux of horizontal pseudomomentum (“momentum flux”) due to gravity waves in satellite temperature data [e.g., Alexander *et al.*, 2008; Wright *et al.*, 2010; McDonald, 2012; France *et al.*, 2012]. However, these studies have

focussed only on the highest-amplitude wavelike signals in each profile, obtaining at most one wave per profile height level and ignoring potentially useful data on colocated waves with smaller amplitudes. These overlapping waves are likely to be numerous and, depending on their physical scale, may individually transport a larger momentum flux than the largest-amplitude events, a key property of GWs that has a major impact on the upper-atmospheric circulation [e.g., Andrews *et al.*, 1987; Fritts and Alexander, 2003].

[4] Here, we adapt the GW detection methodology described by Alexander *et al.* [2008] to allow the detection of colocated wave signals. Section 2 describes the data used and section 3 the method; section 4 then briefly illustrates differences in results between the two methods for a sample period and altitude range, and section 5 discusses the implications and some limitations.

2. HIRDLS

[5] The High Resolution Dynamics Limb Sounder (HIRDLS, Gille *et al.* [2003]) is a limb-scanning radiometer on NASA’s Aura satellite. Designed to measure atmospheric radiances at high vertical resolution throughout the middle atmosphere, after launch an optical blockage obscured a large proportion of the viewing aperture [Barnett *et al.*, 2005]. Due to this, major corrective work has been required to produce useful atmospheric data [Gille *et al.*, 2008].

[6] The current version of the HIRDLS data set, V007, provides vertical temperature profiles from the tropopause up to ~80 km in altitude as a function of pressure [Gille *et al.*, 2012]. The vertical resolution of the instrument is ~1 km throughout most of the vertical range [Wright *et al.*, 2011], dropping to ~2 km above ~60 km, with a precision ~0.5 K throughout the stratosphere. Data are available from late January 2005 until early 2008, when a failure of the optical chopper terminated data collection. We here use data from May 2006; this period is chosen to coincide with Alexander *et al.* [2008].

3. Analysis

3.1. ST Analysis

[7] Initially, we compute the mean background temperature and the first six planetary wave modes for each height level and remove these from the data [Fetzer and Gille, 1994]. This leaves a temperature perturbation profile for each measurement location, which we then interpolate onto a regular 1 km vertical scale, representative of the actual resolution of the instrument at most altitudes. We analyzed each such perturbation profile using the ST and cross-multiply along-track-adjacent profile pairs to produce complex cospectra, from which we compute the covarying temperature amplitude $\hat{T}(\lambda_z, z)$ for each profile-pair.

Additional supporting information may be found in the online version of this article.

¹National Center for Atmospheric Research, Boulder, Colorado, USA.

²Center for Limb Atmosphere Sounding, University of Colorado at Boulder, Boulder, Colorado, USA.

Corresponding author: C. J. Wright, Atmospheric Chemistry Division, National Center for Atmospheric Research, Mitchell Lane, Boulder, CO 80301, USA. (corwin.wright@trinity.oxon.org)

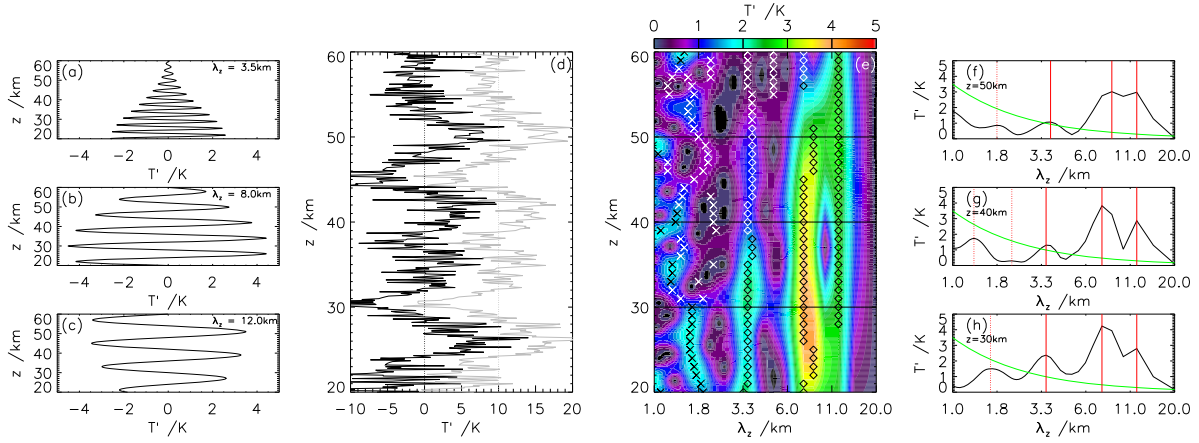


Figure 1. Schematic diagram of the overlapping wave detection process. Figures 1a–1c show three artificial waves, and (d) the sum of these waves combined with 2 K normally-distributed noise (black) and an identical wave with an equivalent but differently-seeded noise distribution, offset by +10 K; vertical dotted lines indicate the zeros of these two profiles. The colored contours of Figure 1e show the absolute ST cospectrum of these signals; open diamonds show local maxima we would accept as wave signals and crosses local maxima which are not accepted. Figures 1f–1h show slices from Figure 1e at three height levels; the black curve shows the ST cospectrum, the green curve a schematic representation of our background estimate $N_{99}(\lambda_z, z)$, solid red lines accepted local maxima and dashed red lines rejected local maxima. The use of black or white symbols in Figure 1e is for contrast only; no difference is implied.

[8] We next compute the horizontal wavelength between adjacent profiles

$$\lambda_h = 2\pi \frac{\Delta r_{i,i+1}}{\Delta \phi_{i,i+1}} \quad (1)$$

and absolute along-track momentum flux [Ern *et al.*, 2004]

$$M_{i,i+1} = \frac{\rho}{2} \frac{\lambda_z}{\lambda_h} \left(\frac{g}{N} \right)^2 \left(\frac{\hat{T}}{\bar{T}} \right)^2, \quad (2)$$

for this signal, where λ_h and λ_z are the horizontal and vertical wavelengths of the signal, $\Delta r_{i,i+1}$ and $\Delta \phi_{i,i+1}$ the geographic and phase differences between adjacent profiles, \hat{T} and \bar{T} the temperature perturbation size and the background temperature, ρ the atmospheric density, N the Brunt-Väisälä frequency, g the acceleration due to gravity, and $M_{i,i+1}$ the estimated momentum flux carried by the signal. In previous studies using this method, this was performed only for the highest-amplitude signal at each height level, but here we instead compute λ_h and hence $M_{i,i+1}$ for each (z, λ_z) at which a distinct local maximum is observed in the ST spectrum. Each of these peaks potentially represents an overlapping wave in the analysis. We perform the ST analysis over the range 15–60 km altitude, but only consider here results in the 20–30 km altitude range; thus, there may be some edge-truncation of longer vertical waves at the bottom of the analysis window where the altitude range extends insufficiently far downwards.

[9] Figures 1a–1e illustrate this process for an artificial case. Figures 1a–1c show three waves, and Figure 1d the sum of these waves combined with normally-distributed noise of peak amplitude 2 K (black) and an identical wave with differently-distributed noise of the same form (gray, offset by +10 K). Figure 1e then shows $\hat{T}(\lambda_z, z)$ derived from the ST cross-spectrum of these two profiles. The overlaid symbols (crosses and diamonds) show local maxima in the spectrum.

3.2. Statistical Significance

[10] A proportion of these wavelike signals are likely to be spurious. So, we must apply some kind of significance check to ensure that we are observing genuine wave signatures.

[11] To do this, we implement a modified version of the significance testing method described by *McDonald* [2012]. In this study, a large number of artificial profile-pairs were generated from an autoregression analysis of normalized (detrended and scaled by their standard deviation) COSMIC [Anthes *et al.*, 2008] profiles. These profile-pairs were then analyzed using the ST and their cospectral amplitudes used to compute a probability distribution of the signals that would be expected to be measured from two uncorrelated profiles.

[12] We make two modifications to this method. First, we use real uncorrelated (non-adjacent) normalized profile-pairs to compute the background distribution. This should not significantly affect the result, but reduces computational complexity and runtime. Second, we compute the distribution on a temporally and spatially localized basis: specifically, we take 2 500 randomly sampled profile-pairs from each 10° latitude by 60° longitude box for each calendar month (that is to say, all Januaries during the HIRDLS mission, all Februaries, etc.), compute the ST cospectrum for each such profile-pair at each height, and from this generate an estimate of the background distribution as a function of λ_z and z . As with *McDonald* [2012], we have conservatively chosen to accept data above the 99th percentile of the probability distribution as valid; this allows us to produce an estimate of the required significance level to treat a signal as a wave $N_{99}(\lambda_z, z)$.

[13] Figures 1e–1h show the results of this process. Figures 1f–1h show, for three height levels, $\hat{T}(\lambda_z)$ (black curve). Overlaid on this in green is a schematic representation of $N_{99}(\lambda_z, z = Z)$: we represent this in each case by the same curve, but in practice it will differ for each height and location. Finally, vertical red lines indicate the local maxima

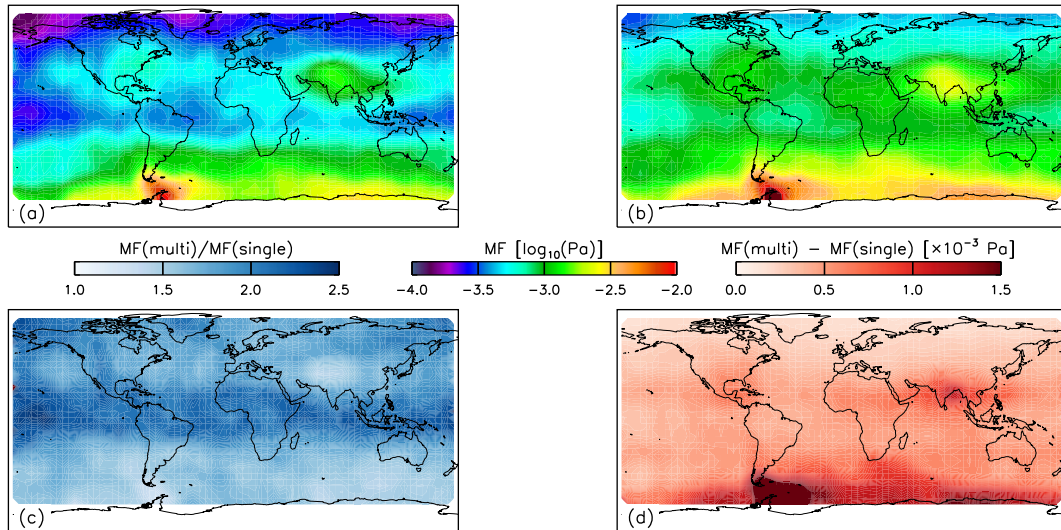


Figure 2. Maps illustrating mean GW $M_{i,i+1}$ for May 2006 over the altitude range 20–30 km. Figure 2a shows values selecting only the highest-amplitude wave in the profile; Figure 2b shows the $M_{i,i+1}$ summed over all statistically significant wave modes. Figure 2c shows the ratio of Figure 2b to Figure 2a and Figure 2d the absolute difference.

found in the ST cross-spectrum; solid lines show maxima above $N_{99}(\lambda_z, z = Z)$ and dashed lines below, which are discarded in our analysis. In each case, we observe peaks of approximately the same wavelength and magnitude as the original input waves; the $\lambda_z = 8$ km wave is slightly shifted in wavelength at some heights due to deficiencies in the transform methodology.

[14] Figure 1e shows this data for the full distribution of $\hat{T}(\lambda_z, z)$: open diamonds indicate peaks above and crosses peaks below the noise level. We see that, in general, the local maxima representing the input waves in Figures 1a–1c are well above the noise level in this case, while those produced by noise or arising due to the sampling spatial frequency are weaker and not retained by our analysis. This will not necessarily be true in all observed cases in real data.

[15] For this idealized example, the proportion of the total input signal variance, including noise, identified as wavelike signals by the peak-only method is 36%, while the all-modes method recovers 48% of the original variance. In the real case, these numbers are lower: for the period and altitude range considered, the global daily mean of recovered variance as a percentage of the input profile variance ranges between ~ 10 –15% for the peak-only method and ~ 17 –25% for the all-modes case.

4. Results

[16] Figure 2a shows a map of the highest-amplitude-wave-mode-only (“peak-only”) results, averaged over the 20–30 km altitude range for May 2006 and gridded onto a $5^\circ \times 5^\circ$ scale. This closely reproduces Figure 4 of *Alexander et al.* [2008] and contrasts with Figure 2b, which shows $M_{i,i+1}$ summed over all statistically significant resolved wave modes (“all-modes”) for the same period and altitude range. Figures 2c and 2d show the ratio and difference, respectively. We observe increased $M_{i,i+1}$ at all locations, with an overall 68% increase in the area-weighted gridded result. The absolute increase is largest over already strong regions such as India, the Southern Ocean, and in particular, the

Antarctic Peninsula. In relative terms, however, the distribution is somewhat different: we see an almost-doubling of measured $M_{i,i+1}$ throughout large parts of the northern hemisphere and tropics, while the increase over most of the southern hemisphere is only $< \sim 1.2\times$.

[17] An equivalent analysis has also been performed for July 2006 (this figure is omitted here for brevity, but is available as auxiliary material to the article): during this period, the Intertropical Convergence Zone has moved north of the equator, producing a narrow band of strong convection which in satellite observations would be expected to peak over Central America and southern China (see e.g., Figure 1b of *Choi et al.*, [2009]). This large convective source would be expected to produce short vertical and horizontal waves, which could be strongly undersampled using the peak-only method. We see an increase in absolute measured $M_{i,i+1}$ over the regions, we expect to be associated with strong GW activity based on the ray-based gravity wave temperature variance predictions of *Choi et al.* [2009] Figure 1b, with enhancements over Asia (stretching out into the Pacific) and Central America, but a relative increase smaller than that in the equatorial tropics or high northern latitudes.

[18] Figure 3 shows the same data as a function of (Figure 3a) λ_z and (Figure 3b) λ_h for 36 geographical regions, each of 60° longitude by 25° latitude, illustrated by maps behind the individual panels. Each panel has been normalized to equal 1 at the peak all-modes $M_{i,i+1}$ for each region. Note that the southernmost region extends geographically to 75°S , but in practice does not include any results poleward of 64°S due to a lack of data. Green curves show the peak-only distribution and blue curves the all-modes distribution; red curves show the difference between these.

[19] Considering first λ_z , Figure 3a, we see marked latitudinal variations in the new distributions (blue). With some exceptions, values in northern polar- and midlatitudes tend to be evenly distributed across the wavelength range or bimodal with both long- and short-wavelength peak. This is in stark contrast to the peak-only results, which were

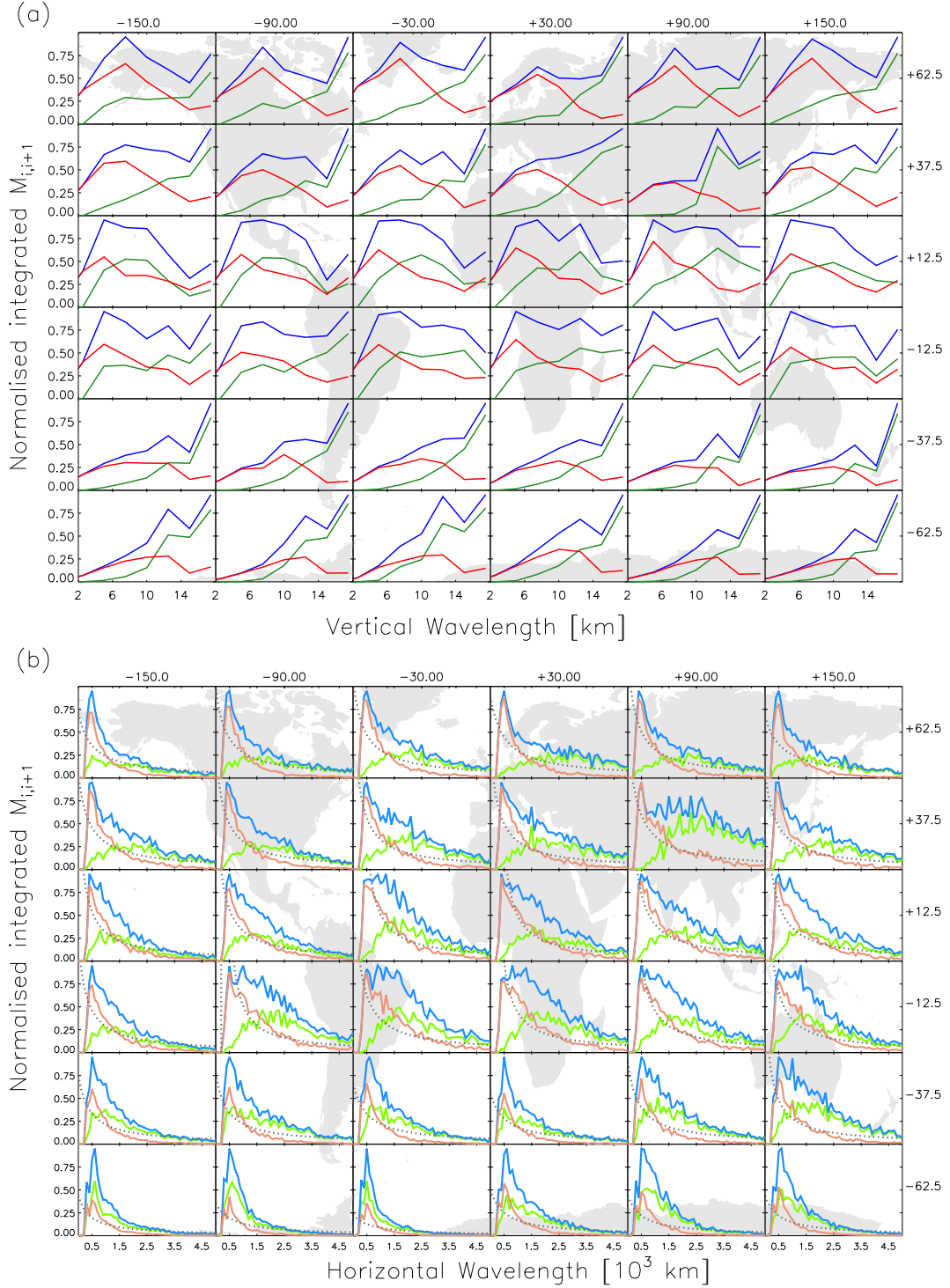


Figure 3. Regional plots illustrating the distribution of measured GW $M_{i,i+1}$ against (a) vertical and (b) horizontal wavelength. Each plot illustrates the 60° by 30° region illustrated in the background. Values are normalized such that the wavelength with the highest $M_{i,i+1}$ in that region equals 1; for absolute $M_{i,i+1}$ values, see Figure 2. For each box, the green curve shows the sum of the $M_{i,i+1}$ carried by the largest wave in each profile, the blue curve the $M_{i,i+1}$ carried by all statistically significant waves, and the red curve the difference between these values. Latitudes and longitudes are indicated by the right and top axes, respectively. Dotted gray lines indicate curves of $1/\lambda_h$, normalized to equal the red curves at their half-maximum.

primarily made up of much longer waves in the vertical. Tropical latitudes, meanwhile, are dominated by short vertical waves, and southern midlatitudes by long vertical waves; the distribution of vertical wavelengths in these regions is

not altered nearly as much, but a much greater proportion of detected $M_{i,i+1}$ is at shorter horizontal wavelengths. Globally, the change in measured $M_{i,i+1}$ (red) is clearly primarily due to the improved detection of small vertical-scale waves, with

the increase in measured $M_{i,i+1}$ largest at short λ_z in all locations. These small waves have only a small relative effect at high southern latitudes, with the additional relative contribution smallest over the orographically dominated Antarctic Peninsula region, but are the main cause of the near-doubling of $M_{i,i+1}$ we saw in Figure 2 at high northern latitudes and over India.

[20] Changes in λ_h , Figure 3(b), are less dramatic but still important: in all regions, additional $M_{i,i+1}$ is contributed by short horizontal-scale waves which were previously not considered, shifting the overall distribution towards lower λ_h . We see a sharp drop at very short λ_h in both the single- and multiple-peak analyses despite the inverse-dependence of $M_{i,i+1}$; this is most probably due to the horizontal spacing of the profiles limiting the detection of very short horizontal waves. There are again significant latitudinal variations: the additional contribution due to short horizontal waves is weakest in relative terms across the Southern Ocean, consistent with the relatively small increase in overall $M_{i,i+1}$ here. Significant additional $M_{i,i+1}$ due to short waves appears at very high northern latitudes.

[21] Detailed satellite maps of the full distribution of measured wavelengths in the literature are few, but we can compare our results in the tropics to those of *Ern and Preusse* [2012]. There, subtropical gravity wave momentum flux (GWMF) spectra are discussed; Figures 2a, 2b, 2e, and 2f show maxima in the GWMF distribution at a $\lambda_z \sim 7$ km and $\lambda_h \sim 500$ km in both deep-convective and non-convective regions for both southern and northern subtropical latitudes, with the majority of results falling within a range $\lambda_z \sim 5$ –15 km and $\lambda_h \sim 400$ –1200 km. These correspond geographically to the two bands on either side of the equator in our Figures 3a and 3b; here, our all-modes distributions show peaked regions corresponding to, very approximately, ~ 4 –12 km in the vertical and ~ 400 –1500 km in the horizontal, peaking at ~ 4 –6 km and ~ 500 km, respectively. This suggests reasonable agreement despite the methodological differences and the different time periods studied.

5. Discussion and Conclusions

[22] This method still has important limitations. As we saw in Figure 1, closely-spaced peaks in the ST cospectrum can merge to form mis-measured peaks, and a smaller wave in the same region as a large one but with much smaller amplitude will tend to be “swamped” by the larger signal. Also, the observed increase in actual momentum flux may in practice be smaller than our measured increase in $M_{i,i+1}$: since we sample only the absolute rather than the vector momentum flux, waves we observe and sum here may in fact cancel out due to different propagation directions. It also does not improve on many of the limitations inherent in the method, such as the observational filter [*Alexander and Barnet*, 2007] of the instrument, or the tendency of the ST to underestimate wave amplitudes [*Wright*, 2010].

[23] Furthermore, the distribution of the additional horizontal wavelengths in Figure 3b often shows similarity to a distribution of $1/\lambda_h$ (indicated by the gray dashed line on each panel). This would equate to a flat distribution in squared-amplitude, as discussed by *Ern et al.* [2004], such a distribution is indicative of a large proportion of the detected signals being from waves shorter than the horizontal

resolution limit of the instrument. These would be aliased in the data, consequently being assigned a too-large horizontal wavelength. This would tend to reduce (equation 2) the estimate of $M_{i,i+1}$ for these additional waves, suggesting that these waves may be a more significant contributor to total $M_{i,i+1}$ than we estimate.

[24] Nevertheless, it does represent a useful improvement on the existing method. Our results show that the inclusion of these previously unconsidered overlapping waves substantially alters the measured GW spectrum, greatly increasing our estimate of globally integrated $M_{i,i+1}$ and enhancing the relative significance of large parts of the globe. This has important implications for the source spectra used in GW model parameterizations. Further study will focus on the changes in the observed GW climatology.

[25] **Acknowledgments.** The authors are currently funded by NASA’s Aura satellite program under contract NAS5–97046. The article was written up during a visit by CJW to the University of Oxford, generously arranged by Prof. Lesley Gray. The authors would also like to thank Dr. Joanna Barstow for useful suggestions on the figures, Dr. Adrian McDonald for advice on the implementation of the statistical-checking methodology and useful questions on some preliminary results, Dr. Scott Osprey for helpful advice, and two anonymous reviewers for useful suggestions. This work benefited from discussions at the International Space Science Institute (ISSI) in Bern, Switzerland.

[26] The National Center for Atmospheric Research is sponsored by the National Science Foundation. Any opinions, findings, and conclusions or recommendations expressed in the publication are those of the authors and do not necessarily reflect the views of the National Science Foundation.

References

- Alexander, M. J., and C. Barnet (2007), Using satellite observations to constrain parameterizations of gravity wave effects for global models, *J. Atmos. Sci.*, *64*(5), 1652–1665, doi:10.1175/JAS3897.1.
- Alexander, M. J., et al. (2008), Global estimates of gravity wave momentum flux from High Resolution Dynamics Limb Sounder (HIRDLS) observations, *J. Geophys. Res.*, *113*, D15S18, doi:10.1029/2007JD008807.
- Alexander, M. J., et al. (2010), Recent developments in gravity-wave effects in climate models and the global distribution of gravity-wave momentum flux from observations and models, *Q.J.R. Meteorol. Soc.*, *136*(650), 1103–1124, doi:10.1002/qj.637.
- Andrews, D. G., C. B. Leovy, and J. R. Holton (1987), *Middle Atmosphere Dynamics, Volume 40 (International Geophysics)*, Academic Press, New York.
- Anthes, R. A., et al. (2008), The COSMIC/FORMOSAT-3 mission: Early results, *B. Am. Meteorol. Soc.*, *89*(3), 313–333, doi:10.1175/BAMS-89-3-313.
- Barnett, J. J., C. L. Hepplewhite, L. Rokke, and J. C. Gille (2005), Mapping the optical obscuration in the NASA Aura HIRDLS instrument, *Proceedings of the SPIE*, *5883*, 11–110, San Diego.
- Choi, H.-J., H.-Y. Chun, and I.-S. Song (2009), Gravity wave temperature variance calculated using the raybased spectral parameterization of convective gravity waves and its comparison with Microwave Limb Sounder observations, *J. Geophys. Res.*, *114*(D8), doi:10.1029/2008JD011330.
- Ern, M., and P. Preusse (2012), Gravity wave momentum flux spectra observed from satellite in the summertime subtropics: Implications for global modeling, *Geophys. Res. Lett.*, *39*(15), 1–5, doi:10.1029/2012GL052659.
- Ern, M., P. Preusse, M. Alexander, and C. D. Warner (2004), Absolute values of gravity wave momentum flux derived from satellite data, *J. Geophys. Res.*, *109*, D20103, doi:10.1029/2004JD004752.
- Fetzer, E. J., and J. C. Gille (1994), Gravity wave variance in LIMS temperatures. part I: Variability and comparison with background winds, *J. Atmos. Sci.*, *51*(17), 2461–2483.
- France, J., V. Harvey, M. Alexander, C. Randall, and J. Gille (2012), High Resolution Dynamics Limb Sounder observations of the gravity wave-driven elevated stratopause in 2006, *J. Geophys. Res.*, *117*(D20), 1–9, doi:10.1029/2012JD017958.
- Fritts, D. C. (1984), Gravity wave saturation in the middle atmosphere: A review of theory and observations, *Rev. Geophys.*, *22*(3), 275–308.
- Fritts, D. C., and M. J. Alexander (2003), Gravity wave dynamics and effects in the middle atmosphere, *Rev. Geophys.*, *41*, doi:10.1029/2001RG000106,1.

- Gille, J., J. Barnett, J. Whitney, M. Dials, D. Woodard, W. Rudolf, A. Lambert, and W. Mankin (2003), The High Resolution Dynamics Limb Sounder (HIRDLS) experiment on Aura, *Proc. of the SPIE*, 5152, 162–171, doi:10.1117/12.507657.
- Gille, J., et al. (2008), High Resolution Dynamics Limb Sounder: Experiment overview, recovery and validation of initial temperature data, *J. Geophys. Res.*, 113, D16S43, doi:10.1029/2007JD008824.
- Gille, J. C., et al. (2012), High Resolution Dynamics Limb Sounder Earth Observing System (EOS): Data Description and Quality Version 7. [Available from <http://www.eos.ucar.edu/hirdls/data/>].
- McDonald, A. J. (2012), Gravity wave occurrence statistics derived from paired COSMIC/FORMOSAT3 observations, *J. Geophys. Res.*, 117(D15), 1–12, doi:10.1029/2011JD016715.
- Richter, J. H., F. Sassi, and R. R. Garcia (2010), Toward a physically based gravity wave source parameterization in a general circulation model, *J. Atmos. Sci.*, 67(1), 136–156, doi:10.1175/2009JAS3112.1.
- Song, I.-S., H.-Y. Chun, R. R. Garcia, and B. a. Boville (2007), Momentum flux spectrum of convectively forced internal gravity waves and its application to gravity wave drag parameterization. Part II: Impacts in a GCM (WACCM), *J. Atmos. Sci.*, 64(7), 2286–2308, doi:10.1175/JAS3954.1.
- Stockwell, R. G., L. Mansinha, and R. P. Lowe (1996), Localization of the complex spectrum: The S Transform, *IEEE T. Signal. Proces.*, 44(4), 998–1001.
- Wright, C. J. (2010), Detection of stratospheric gravity waves using HIRDLS data, Ph.D. thesis, University of Oxford. [available from <http://ora.ouls.ox.ac.uk/objects/uuid:ef4aa65d-67c1-43ac-90de-1b5bda6c8230>].
- Wright, C. J., S. M. Osprey, J. J. Barnett, L. J. Gray, and J. C. Gille (2010), High Resolution Dynamics Limb Sounder measurements of gravity wave activity in the 2006 arctic stratosphere, *J. Geophys. Res.*, 115, D02105, doi:10.1029/2009JD011858.
- Wright, C. J., R. Belmonte M., and J. C. Gille (2011), Intercomparisons of HIRDLS , COSMIC and SABER for the detection of stratospheric gravity waves, *Atmos. Meas. Techniques*, 4(8), 1581–1591, doi:10.5194/amt-4-1581-2011.